

Relating the L-H Power Threshold Scaling to Edge Turbulence Dynamics

Z. Yan¹, G.R. McKee¹, J.A. Boedo², D.L. Rudakov², L. Schmitz³, P.H. Diamond³, G. Tynan³,
R.J. Fonck¹, R.J. Groebner⁴, T.H. Osborne², and P. Gohil⁴

¹*University of Wisconsin-Madison, Madison, Wisconsin 53706-1687, USA*

²*University of California San Diego, La Jolla, California 92093, USA*

³*University of California Los Angeles, Los Angeles, California 90005, USA*

⁴*General Atomics, P.O. Box 85608, San Diego, California 92186-5608, USA*

Abstract. Understanding the physics of the L-H transition power threshold scaling dependencies on toroidal field and density is critical to operating and optimizing the performance of ITER. Measurements of long-wavelength ($k_{\perp}\rho_i < 1$) turbulent eddy dynamics, characteristics, flows, and flow shear in the near edge region of DIII-D plasmas have been obtained during an ion gyro-radius scan (varying toroidal field and current) and density scan in a favorable geometry (ion ∇B drifts towards the X-point), in order to determine the underlying mechanisms that influence the macroscopic L-H power threshold scaling relations. It is found that the normalized integrated long wavelength density fluctuation amplitudes (\tilde{n}/n) in the pedestal increases with ρ^* approaching the L-H transition. The turbulence poloidal flow spectrum evolves from Geodesic Acoustic Mode (GAM) dominant at lower power to Low-Frequency Zonal Flow (LFZF) dominant near the L-H transition, and the effective shearing rate correspondingly increases. An inferred Reynolds Stress, $\langle \tilde{v}_r(t)\tilde{v}_\theta(t) \rangle$, from BES velocimetry (inferring velocity field from imaging) measurements is found to significantly increase near the L-H transition. Similar observations are made with the Langmuir probe measurements. At lower electron density, a clear increase of the LFZF is observed prior to the L-H transition, which is not evident at higher density. Taken together, these results are qualitatively/semi-quantitatively consistent with the electron density and toroidal field scaling of the L-H transition power threshold.

PACS Numbers: 52.55.-s, 52.55.Dy

1. Introduction

Accessing H-mode and maintaining H-mode performance levels are critical to ITER operation. For years, work has been focused on determining the requirements for access to H-mode in various machines. It has been found that the L-H transition power threshold increases with toroidal field and density, $P_{LH} = 0.049 B_t^{0.8} n_e^{0.72} S^{0.94}$ [1]. However, it has been found in many machines that there is a minimum in the density dependence of the power threshold. As the density is further lowered below a particular minimum value, the L-H transition power threshold increases. This density value corresponding to minimum power threshold may be a function of toroidal field. Besides the toroidal field and density dependence included in the well-known scaling relation, the L-H transition power threshold is also a strong function of toroidal rotation [2], ion species [3-5], divertor magnetic geometry [6], etc. The underlying physics behind these so-called ‘hidden parameters’ has not been identified. Understanding such physics is clearly very important for achieving the high performance goals for ITER.

In order to investigate the physical mechanisms behind these dependencies, a set of L-H transition experiments has recently been performed on DIII-D that focuses on investigating the dependence of local edge parameters on toroidal field and density near the L-H threshold. These experiments were performed in favorable geometry (ion ∇B drifts towards the X-point) deuterium plasmas with scans of normalized ion gyroradius (maintaining edge dimensionless parameters nearly fixed except for ρ^* , $\rho^* = \rho_l/a$) and density. The existence of the Geodesic Acoustic Mode (GAM) and the Low Frequency Zonal Flow (LFZF) has been clearly identified experimentally in tokamak and stellarator plasmas [7, 8]. Those flows are predicted to be generated by the plasma turbulence and may relate to the shear flow mechanism thought to drive the L-H transition [9]. In this work, turbulence dynamics and characteristics were measured at the plasma edge to investigate how the edge turbulence

dynamics impact the L-H transition scaling. This paper presents the experimental conditions, turbulence characteristics and scaling behavior from these experiments and relates them to the L-H transition power threshold.

2. Experimental Set Up

The experiments for the ion gyroradius scan were performed with a downward biased double-null magnetic configuration. The direction of the applied toroidal magnetic field produced an ion grad-B drift towards the lower X-point. The auxiliary heating is co-current neutral beam injection. The toroidal field was varied from 1T to 2T with current ranging from 0.5 MA to 1 MA. The edge safety factor q_{95} was held nearly fixed at 5. The other non-dimensional parameters such as collisionality ν^* (~ 1), T_e/T_i (~ 0.7) were kept nearly constant at the pedestal top in the L-mode phase just before the L-H transition by appropriately varying the injected beam power and the gas fueling. The L-H transitions were obtained by slowly increasing the NBI heating power.

A separate experiment was performed to vary density in a similar plasma shape at fixed toroidal field of 2T and current of 1MA. Line-averaged electron density in the L-mode phase before the L-H transition was varied from $1.7 \times 10^{19} \text{ m}^{-3}$ to $4.3 \times 10^{19} \text{ m}^{-3}$. Fig. 1 (a,b) show some basic plasma parameters for these two experiments.

For both experiments, an 8×8 2D array of high sensitivity Beam Emission Spectroscopy (BES) was located in the plasma edge region ($\rho \sim 0.85-1.0+$) providing long wavelength ($k_{\perp} \rho_l < 1$) density fluctuation measurements before, during and after the L-H transition. Fig. 2 displays the plasma equilibrium plots for different parameter scans with the BES 2D array overlaid.

3. Toroidal Field Dependence of Power Threshold and Turbulence Dynamics

In order to understand how the evolution of turbulence and flows with time impacts the transition, it is interesting to compare the turbulence dynamics at different times relative to

the L-H transition for different plasma conditions. For this purpose, long wavelength density fluctuation measurements from BES were analyzed for two toroidal fields (two ρ^* values) at two 10 ms time windows, one well before the L-H transition (~ 300 ms before) and the other near the L-H transition (10 ms before). The transition power threshold is about 2 MW for $B_t=2T$ and 1.1MW for $B_t=1T$. Notably, these transitions occur directly from L-mode to H-mode with no Limit-Cycle-Oscillation (LCO) phase, which has been observed in some other experiments [10, 11].

Fig.3 shows the profile of the relative density fluctuation amplitudes (\tilde{n}/n) integrated over 20k-150kHz (where broadband fluctuations exist) at the time near the transition for the two ρ^* values. It is found that the relative density fluctuation amplitudes increase with ρ^* approaching the L-H transition except for the outmost position at $\rho\sim 1$. This higher normalized turbulence amplitude at lower toroidal field (higher ρ^*) may provide stronger drive for zonal flows if the phase of the turbulent velocity fields has little changes. These zonal flows are thought to play a dominant role in triggering the L-H transition [12].

An imaging velocimetry technique [13] was applied to the 2D BES measurements to obtain the instantaneous radial and poloidal velocity fields of the turbulent eddy structures. The application of this technique and the inferred velocity dynamics have been compared with the Langmuir probe measurements during the LCO experiments, which provide reasonably good agreement [14]. The 2D BES density fluctuation measurements were first frequency-filtered in the range of 50kHz to 150kHz for each spatial channel, where the fluctuations are measured, before application of the velocimetry algorithm. The velocimetry method itself adds no further frequency filtering. Fig.4 (a) shows an example of such a turbulent velocity field, indicated by the arrows overlaid on a one microsecond 2D BES density fluctuation image snapshot. To examine the turbulence and zonal flow dynamics, the poloidal velocity component from the velocimetry analysis is isolated and spectrally

analyzed. The velocity spectrum of this turbulent velocity field is obtained via ensemble-averaging FFT power spectra over a 10 ms time window at different times relative to the L-H transition, as shown in Fig. 4 (b, d) for both low and high ρ^* conditions at $\rho \sim 0.94$. It is found that in both cases, an increase of the lower frequency component of the turbulence poloidal flow spectrum is observed as the discharge evolves from well before the L-H transition to near the transition. Furthermore, the velocity spectrum evolves from being Geodesic Acoustic Mode (GAM) dominant at lower input power to being Low-Frequency Zonal Flow (LFZF) dominant near the L-H transition. From the measured turbulence velocity field we can infer the Reynolds stress profiles $\langle \tilde{v}_r(t)\tilde{v}_\theta(t) \rangle$ at the different times and different ρ^* , which are shown in Fig. 4 (c, e). It is found that the inferred Reynolds stress gradient increases in the pedestal region approaching the L-H transition for both cases. The gradient of the Reynolds stress is predicted to drive zonal flows [12]. The increase of the Reynolds stress gradient is consistent with the observation of the increase of LFZF-like flow component near the L-H transition in the context of theoretical predictions for L-H transition dynamics. The lower frequency and higher amplitude of the LFZF relative to the GAM suggests a stronger shear state near the transition [12], suggesting the observed increase in Reynolds stress and zonal flows may be playing a role in triggering the transition.

The equilibrium turbulence poloidal flows were also obtained by taking a time average of the instantaneous poloidal velocity at the two 10 ms time windows. Figure 5 compares this time-averaged turbulence poloidal velocity for different times relative to the L-H transition for different ρ^* values. A significant increase of the equilibrium flow shear is clearly observed near the L-H transition relative to the earlier time. From this flow profile, a shearing rate can be estimated as a gradient between the two adjacent radial positions. This shearing rate is compared with the decorrelation rate measured from BES, which is shown in Fig. 6. It is found that the decorrelation rate of the 50 k-150 kHz long wavelength density fluctuations

does not change much with time. However, the shearing rate increases significantly approaching the L-H transition and exceeds the decorrelation rate. Therefore, the shearing rate is strong enough to suppress the turbulence and transport, consistent with triggering the L-H transition. This happens for both low and high ρ^* . It suggests that at higher ρ^* (lower toroidal fields), a lower input power is needed to generate sufficient turbulence amplitude to drive a strong enough flow shear to trigger the L-H transition.

4. Density Dependence of Power Threshold and Turbulence Dynamics

A density scan was performed to examine the turbulence behavior approaching L-H transition as a function of density. In similarly shaped and neutral beam injection heating plasmas used in the ρ^* scan experiment ($B_t=2T$ and $I_p = 1MA$), the line averaged density in the L-mode phase just before the L-H transition was varied over four values, $1.7 \times 10^{19} m^{-3}$, $2.3 \times 10^{19} m^{-3}$, $3.8 \times 10^{19} m^{-3}$ and $4.3 \times 10^{19} m^{-3}$. The transition power thresholds for these densities are about 2.5MW, 2.5MW, 3.7MW and 5MW respectively. Fig. 7 is a plot of the radial profile of the relative density fluctuation amplitudes frequency integrated over 30 kHz-150 kHz for these four density conditions. The normalized density fluctuations (\tilde{n}/n) are similar for the two lower densities, which are lower than the values at the two higher densities. One can speculate that at higher densities, the collisional damping for the zonal flows is higher, which may in turn increase the power threshold. Applying the same velocimetry technique described in the previous section to the 2D BES density fluctuation measurements, we again obtained the instantaneous radial and poloidal velocity fields. Figure 8 shows the spectra of the turbulence poloidal velocity field at $\rho \sim 0.91$. It is found that for the low-density cases ($1.7-2.3 \times 10^{19} m^{-3}$) there is a clear increase of the LFZF-like flow component as the plasma evolves towards the L-H transition. The spectra again evolve from being GAM dominant to being LFZF dominant near the transition, as observed in the ρ^* scan plasmas. However, there

is no evident observation of increase of the LFZF-like flow component at the higher density cases ($3.8-4.3 \times 10^{19} \text{m}^{-3}$). Moreover, no GAM was observed at these higher densities, which may be consistent with the higher collisional damping of the zonal flows at higher density suppressing GAM. It is important to note that at the two higher density conditions there is no evidence for a LFZF-like flow in the measured velocity spectra. This may suggest that any LFZF is below detectable limits for the velocity inference technique applied here. However, we also note that the time window used for this analysis averages over 10 ms before the transition. It is possible that faster dynamics may take place immediately before the transition than can be resolved with the 10ms time window. Further analysis of the time evolution of turbulence and flow leading to the transition using analysis techniques under development may be required.

The equilibrium turbulence poloidal flow at the time near the L-H transition was obtained by evaluating the time delay cross correlations between the poloidally separated BES density fluctuation measurements. Figure 9 is a plot of the profile of such flow for the four different densities at the time well before the L-H transition, and Fig.10 is at the time near the transition. It is clearly observed that at the two lower densities there is a much higher shear near $\rho \sim 0.9$ than that at the two higher densities, and this shear is larger than the shear at the earlier time. Fig. 11 and Fig.12 are profiles of the shearing rates estimated as the radial gradient of the adjacent poloidal velocities ($\Delta v_\theta / \Delta r$) from Fig.9 and Fig.10 and the corresponding turbulence decorrelation rates measured from BES. It is found at the time well before the transition the shearing rate is comparable with the decorrelation rate for all four densities, while at the time close to the L-H transition the local shearing rate at $\rho \sim 0.9$ is much larger than the turbulence decorrelation rate at the two lower densities but comparable at the two higher densities. These observations suggest that the combination of the increased turbulence flow shear and zonal flow shear facilitate the L-H transition at lower density,

qualitatively consistent with the P_{LH} density scaling relation. However, to draw a quantitative conclusion of the threshold dependence, an analysis of the nonlinear energy transfer from turbulence into flow via Reynolds stress need to be investigated and will be reported in a future publication.

5. Summary

These results of the edge turbulence dynamics scaling with toroidal field and density across the L-H transition are qualitatively consistent with the L-H transition power threshold dependence on density and toroidal field. At lower toroidal field (higher ρ^*), larger normalized turbulence amplitude is generated, which is predicted to drive stronger zonal flows and corresponding flow shear which can facilitate the L-H transition at a lower input power. Similarly, the stronger flow shear observed at lower density favors the L-H transition at correspondingly lower input power. It is hypothesized that increased turbulence at high power flux drives a stronger Reynolds stress; the Reynolds stress gradient then drives increased zonal flows, which can then trigger the L-H transition through shear flow decorrelation of turbulence. Future studies will include quantitative investigation of the nonlinear energy transfer leading to the L-H transition in various conditions; the turbulence dynamics corresponding to the previously observed increase of the L-H transition power threshold with density falling below the minimum power threshold value; other factors such as X-point height dependence and edge neutral recycling.

This work was supported by the US Department of Energy under DE-FG02-89ER53296, DE-FG02-07ER54917, DE-FG02-08ER54984, and DE-FC02-04ER54698.

References

- [1] E J Doyle et al. Progress in the ITER Physics Basis Chapter 2: Plasma Confinement and Transport 2007 *Nucl. Fusion* **47** S18
- [2] McKee, G.R. et al 2009 *Nucl. Fusion* **49**, 115016
- [3] Gohil, P. et al 2009 *Nucl. Fusion* **49**, 115004
- [4] Gohil, P. et al 2010 *Nucl. Fusion* **51**, 103020
- [5] Ryter, F. et al 2009 *Nucl. Fusion* **49**, 062003
- [6] Carlstrom, T.N. et al 1998 *Plasma Phys. Control Fusion* **40**, 669
- [7] Mckee, G.R. et al 2003 *Phys. Plasmas*, **10**, 1712
- [8] Fujisawa, A. et al 2004 *Phys. Rev. Lett.*, **93**, 165002
- [9] Burrell, K.H. 1997 *Phys. Plasmas* **4**, 1499, 1997
- [10] G. D. Conway, et al., *Phys. Rev. Lett.* 106, 065001 (2011).
- [11] L. Schmitz, *Phys. Rev. Lett.* 108, 155002 (2012).
- [12] Diamond, P.H. et al 2005 *Plasma Phys. Control Fusion* **47**, R35
- [13] McKee, G.R. et al 2004 *Rev. Sci. Instrum.* **75**, 3490
- [14] G. R. Tynan, et al, *Nuclear Fusion*, accepted, (2013).

Figure Captions

Fig.1(a). Ion gyroradius scan and (b) density scan basic parameters (i) D_α signal, (ii) line-averaged density, (iii) pedestal pressure and (iv) q_{95}

Fig. 2. Plasma equilibrium plots with BES array overlaid.

Fig. 3. Integrated density fluctuation amplitudes for $B_f = 2 T$ (black) and $B_f = 1 T$ (blue).

Fig.4(a). A snap shot of the density fluctuation imaging from 2D BES measurement overlaid by the turbulent velocities (black arrows) from velocimetry technique; turbulence poloidal flow spectrum at (b) $B_f = 2 T$ and (d) $B_f = 1 T$, and inferred Reynolds stress profile at (c) $B_f = 2 T$ and (e) $B_f = 1 T$, with black for the time well before L-H transition and red for the time near transition.

Fig. 5(a). Equilibrium turbulence poloidal velocity profile at $B_f = 2 T$ for the time well before the L-H transition (black) and near the transition (red); (b) Equilibrium turbulence poloidal velocity profile at $B_f = 1 T$ for the time well before the L-H transition (black) and near the transition (red).

Fig. 6. Turbulence flow shearing rate (black diamond) and decorrelation rate (red triangle), both obtained from 2D BES turbulence measurements for (a) $B_f = 2 T$ at time well before the transition; (b) $B_f = 2 T$ at the time near the L-H transition; (c) $B_f = 1 T$ at the time well before the transition and (d) $B_f = 1 T$ at the time near the L-H transition.

Fig.7 The frequency integrated density fluctuations for four different densities, $n_e=1.7 \times 10^{13} \text{cm}^{-3}$ (black), $n_e=2.3 \times 10^{13} \text{cm}^{-3}$ (red), $n_e=3.8 \times 10^{13} \text{cm}^{-3}$ (blue), and $n_e=4.3 \times 10^{13} \text{cm}^{-3}$ (dark red)

Fig. 8. Spectrum of the turbulence poloidal velocity field for (a) $n_e = 1.7 \times 10^{19} m^{-3}$, (b) $n_e = 2.3 \times 10^{19} m^{-3}$, (c) $n_e = 3.8 \times 10^{19} m^{-3}$, and (d) $n_e = 4.3 \times 10^{19} m^{-3}$. For each panel black is the time well before the L-H transition and red is for the time near the transition.

Fig.9 Turbulence poloidal flow profiles for four densities at a time well before the L-H transition

Fig. 10. Turbulence poloidal flow profiles for different densities at the time near L-H transition.

Fig. 11 Turbulence decorrelation rate and poloidal flow shearing rate for four densities at the time well before the transition

Fig.12 Turbulence decorrelation rate and poloidal flow shearing rate for four densities at a time near the transition

List of Figures

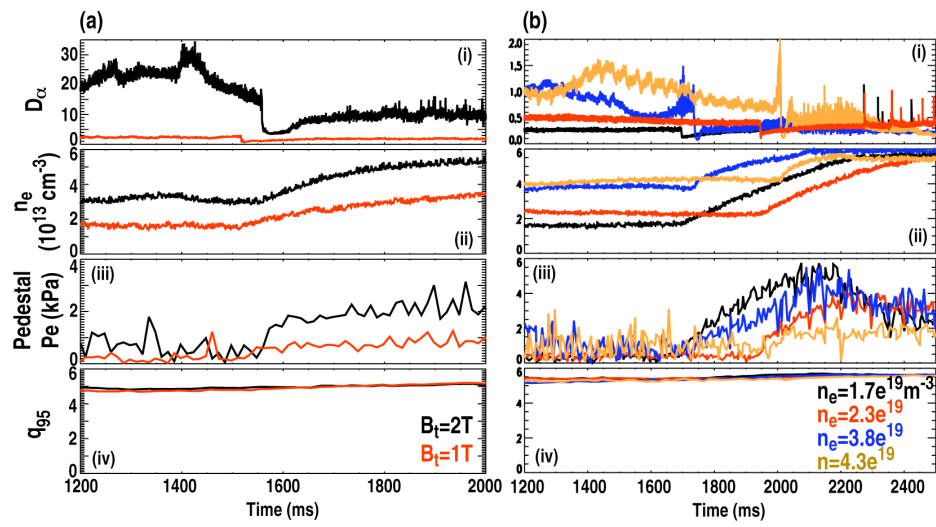


Fig. 1

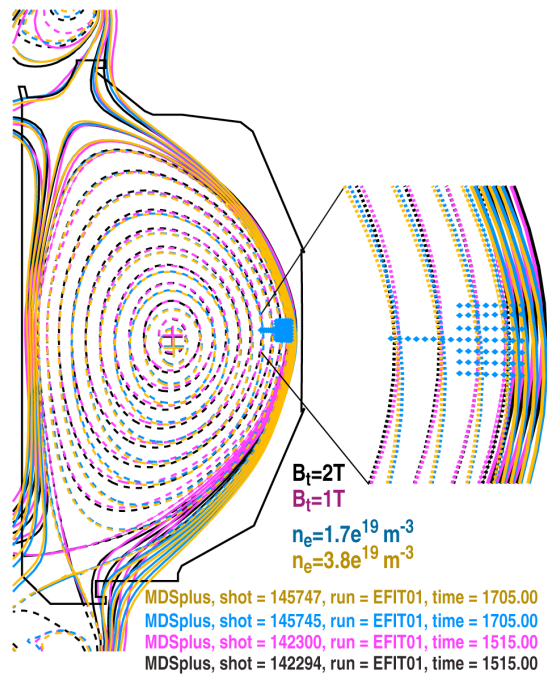


Fig. 2

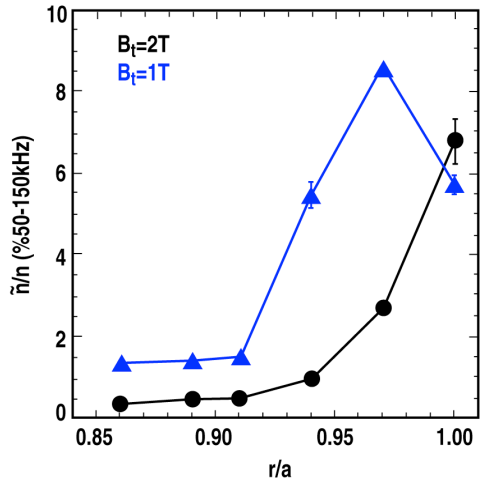


Fig. 3

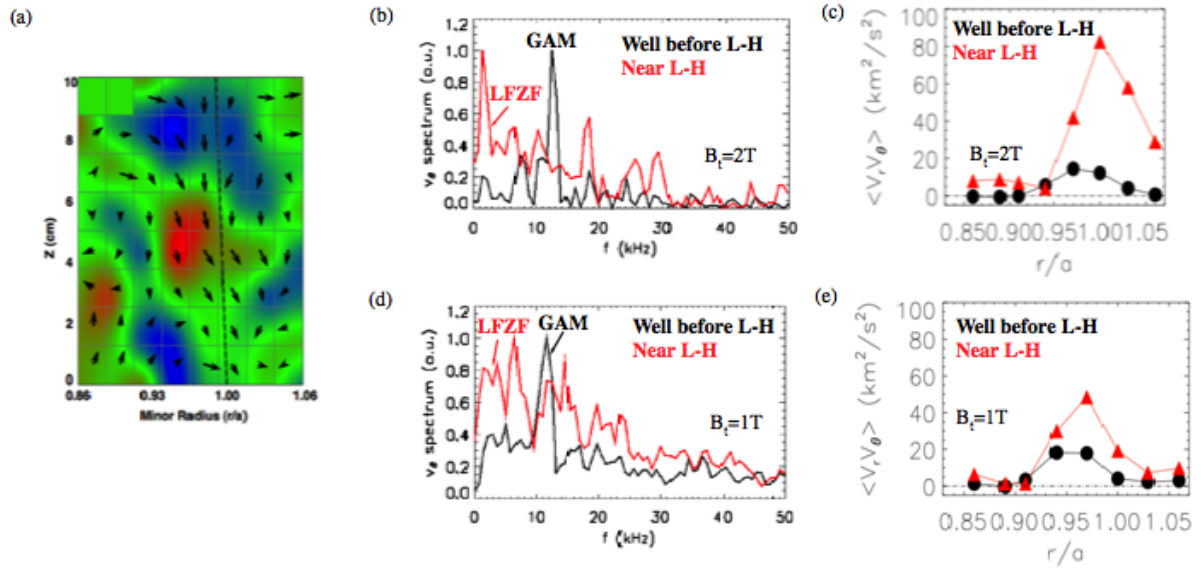


Fig. 4

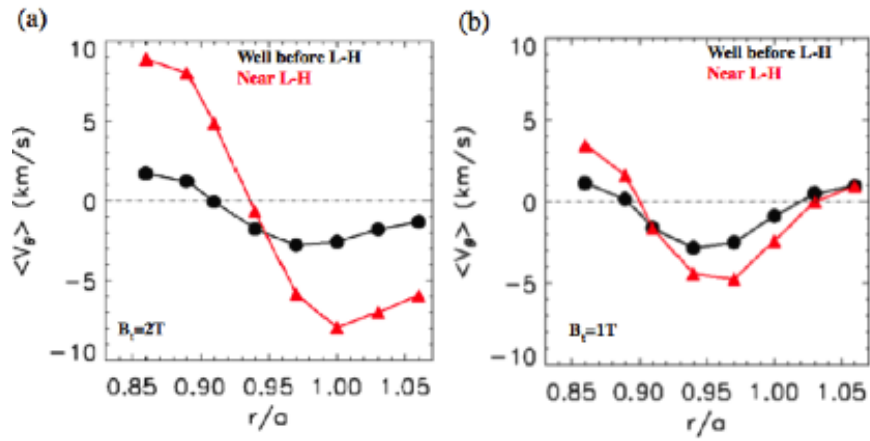


Fig. 5

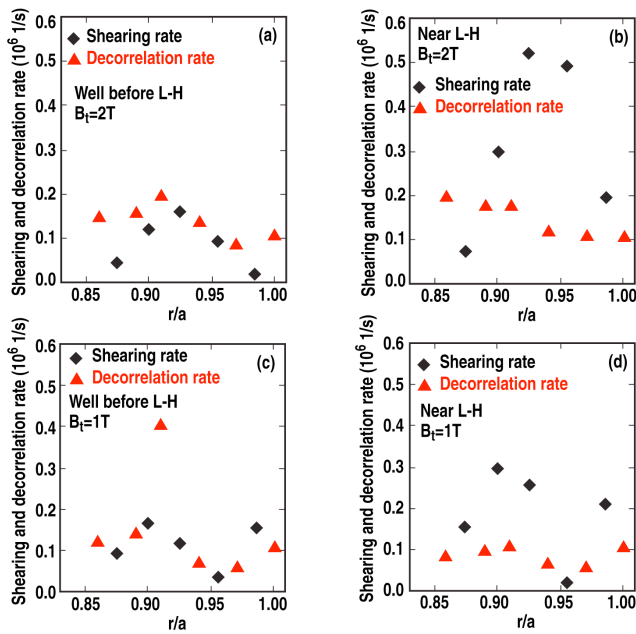


Fig. 6

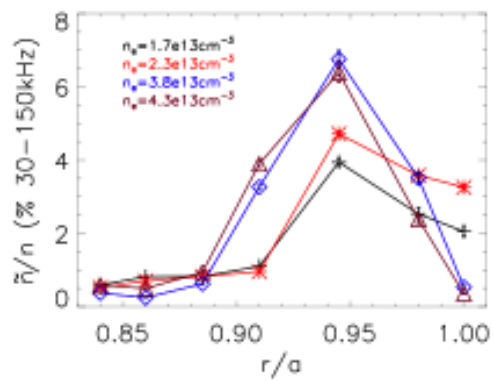


Fig. 7

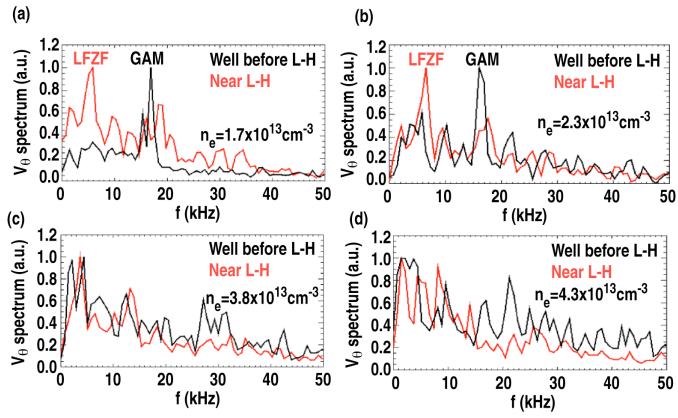


Fig. 8

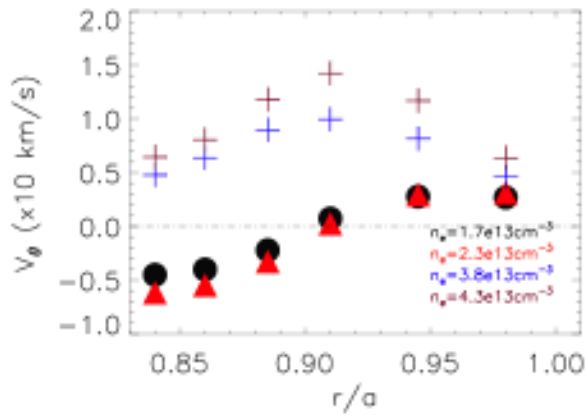


Fig.9

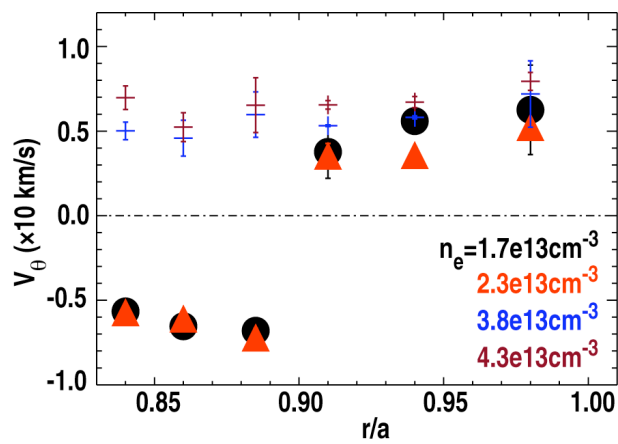


Fig. 10

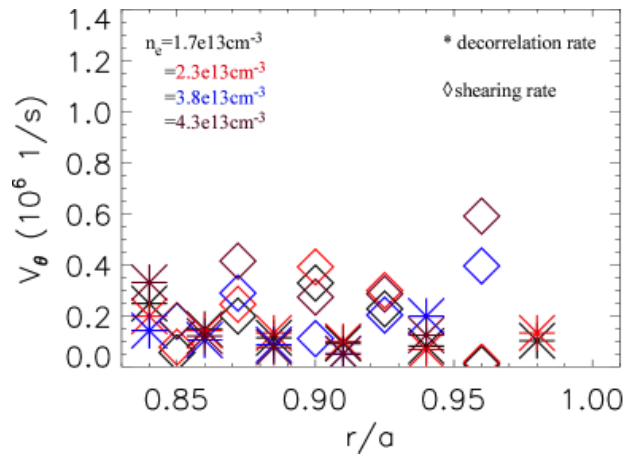


Fig.11

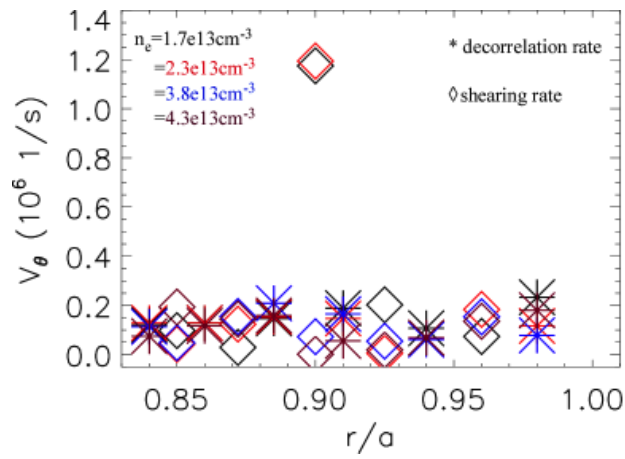


Fig.12